ACS APPLIED ENERGY MATERIALS

www.acsaem.org

Article

Insights into Reaction Mechanisms in Liquid Metals from Density Functional Theory: CH_4 Pyrolysis in BiNiX (X = Cu, Al) Molten Metals as a Case Study

Arda Erbasan, Hande Ustunel,* Daniele Toffoli, Iskender Gokalp, Gulfeza Kardas, and Gokhan Celik

Cite This: *ACS Appl. Energy Mater.* 2024, 7, 3220−3233

Read Online

ACCESS | Metrics & More | Article Recommendations | Supporting Information

ABSTRACT: Pyrolysis of methane using molten metal catalysts in bubble column reactors presents a cleaner and coking-free alternative for hydrogen production from natural gas due to its lack of direct CO_2 emissions. Bubble column reactors overcome coking as the byproduct carbon material floats to the top due to its lower density with respect to the molten metal and can be collected by physical means. Typically, the catalysts used in these systems consist of a low-melting-point solvent metal such as Sn or Bi, along with a higher melting point active component such as Ni. In this study, we present a first-principles investigation that explores the impact of a third component, a promoter, on the reactivity of a Bi−Ni molten alloy. Specifically, we examine Al and Cu as promoters and compare their effects. Unlike previous literature that mostly relies on static nudged elastic bands and free-energy-based calculations, we develop a comprehensive ab initio molecular dynamics-based protocol to provide a detailed account of the reaction mechanism. Our direct rate calculations reveal that, overall, including either promoter at 10 or 20% leads to a better performance than using an unpromoted Ni−Bi binary alloy. To overcome the intrinsic difficulties associated with rate calculations, we have performed a large number of ab initio molecular dynamics calculations and have analyzed the H dissociation times for each reaction step involved in the reaction mechanisms. Our findings reveal that overall Cu outperforms Al as a promoter under the simulation conditions employed. To better understand this outcome, we carefully examined each dissociation event and identified several intriguing trends, including the contrasting contributions of Al and Cu to reactivity. We have further rationalized our results with the help of simple descriptors such as binding energy and partial Bader charges in binary metal clusters and have found that the strength of the interaction of different metal species in the alloy with one another and the product fragments in the immediate neighborhood of the reaction as well as relative partial charges correlate very well with dissociation time data. The analysis methods developed in this study will be used in future research, enabling the screening of a broader range of promoters and facilitating the design of these promising energy production systems.

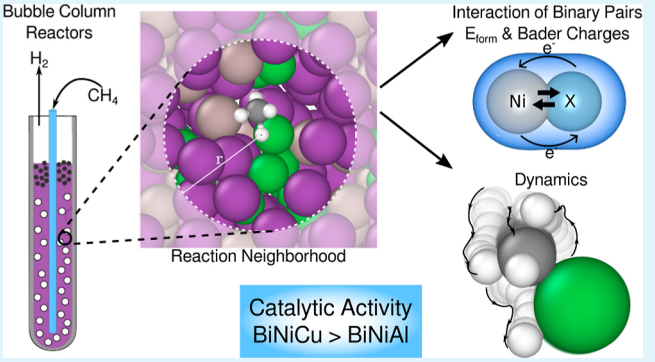

KEYWORDS: *methane pyrolysis, bubble column reactor, molten metal alloy, promoter, density functional theory, ab initio molecular dynamics*

1. INTRODUCTION

In recent years, hydrogen has emerged as a versatile energy carrier and a pivotal fuel source in the global pursuit of clean and sustainable energy.[1] Hydrogen gas can be obtained via various methods of extraction, such as water splitting,[2] biomass or coal gasification,[3] and natural gas reforming.[4] Hydrogen not only holds the potential to replace carbon-based fuels but also finds extensive applications in ammonia and urea production, methanol synthesis, in refineries, and pipelines.[5] However, the majority of the current demand is met through methods that release vast amounts of CO_2 into the atmosphere. According to the Global Hydrogen Review 2023 by IEA,[6] almost all of the current H_2 demand (95 Mt in 2022) is sourced from fossil fuels (>99%), whereas water electrolysis produces less than 100 kT H_2 in 2022. Fossil fuel reforming, primarily utilizing methane (CH_4), is widely employed due to its energy efficiency[1,7,8] but it releases CO_2 as a byproduct. A promising alternative is the CO_2-free CH_4 pyrolysis,[9,10] which is still in the precommercial optimization phase. While it is true that global reserves of natural gas, which serves as the primary source of methane, are also limited, pyrolysis presents itself as an excellent transitional and clean alternative. It offers a viable

Received: December 26, 2023
Revised: March 2, 2024
Accepted: March 6, 2024
Published: April 2, 2024

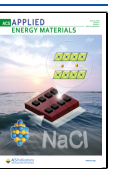

solution until our energy consumption becomes sufficiently independent of fossil fuel resources.

Methane pyrolysis is the decomposition of methane at high temperatures in the absence of oxygen described by the following reaction

$$CH_4 \rightarrow C + 2H_2 \qquad \Delta H_{rxn} = 74.5\ \text{kJ/mol}\ CH_4 \tag{1}$$

When realized noncatalytically, the reaction mechanism exhibits intricate coupling steps with a branching structure that becomes progressively more complex as the reaction progresses.[11,12] Conversely, when a solid-phase catalyst is employed, the proposed mechanism typically follows a simpler sequence of H dissociation steps[10]

$$CH_4^* \rightarrow CH_3^* + H^* \tag{2}$$

$$CH_3^* \rightarrow CH_2^* + H^* \tag{3}$$

$$CH_2^* \rightarrow CH^* + H^* \tag{4}$$

$$CH^* \rightarrow C^* + H^* \tag{5}$$

where the asterisk (*) represents species adsorbed on the surface. As the reactions progress, the resulting H atoms from the dissociation steps combine to form H_2 gas. An alternative dissociation mechanism to the one shown above in eqs 2−5 involves the initial dissociative adsorption of CH_4 over two vacant sites to produce $CH_3^\bullet$ and $H,^\bullet$[13] while the remaining steps of the mechanism are the same.

As catalytic methane pyrolysis is already in extensive use in several traditional applications besides hydrogen production (such as the catalytic growth of carbon nanotubes and other carbon filaments[14]), a wide range of heterogeneous catalysts have already been explored. Notably, Co-based,[15] Ni-based,[16] and Fe-based[17] catalysts and their alloys[18] have been utilized over the years. Among them, Ni-based catalysts have demonstrated exceptional activity compared to others.[19] One significant drawback, however, is the rapid deactivation of these solid-state catalysts by the carbon byproduct presence, which hampers the feasibility of this method.[9,19,20]

Several strategies have been developed to address the coking problem, to control the morphology of the carbon product, and to improve the reactivity of the Ni component. Some of these methods include the careful design of the support material to increase the dispersion of the active metal,[21,22] modifying the composition of the catalytic alloys,[23] and employing promoters.[24] Another effective solution to these issues is the use of molten metals and molten salts, which was proposed at the end of the 1990s. One of the earliest designs, developed by Steinberg,[25] utilizes molten tin or copper. This concept was subsequently implemented by Serban et al.[26] and other researchers[27−31] with the use of bubble column reactors. These reactors are constructed as vertical columns containing the molten metal catalyst.[28] CH_4 gas is released or injected through a sparger. As the ascending methane bubbles interact with the catalysts, the reaction occurs catalytically at the gas−liquid interface. The carbon byproduct, due to its lower density, floats to the catalytic surface of the metal and can be collected, regenerating the catalyst.[19,32] The resulting carbon byproduct can take various forms, such as active carbon, carbon nanotubes, and graphitic materials,[33] which have applications across various industries. Even in cases where the carbon byproduct cannot be used, it can still be safely stored.[34] However, the extent to which these carbon-based materials can be used will be one of the factors that determines the overall feasibility of the method.

The main challenge presented by the bubble reactor design is the high temperatures required for the molten phase of the metal. Upham et al.[35] tested the catalytic activity of some low-melting-point solvent metals and detected some activity, albeit low, in the order In < Bi < Sn < Ga < Pb. The addition of a small amount of an active metal, in particular Ni, was seen to increase the reaction rate, depending on the solvent metal used, without raising the melting temperature significantly. The optimal composition for maximizing reactivity was identified as $Ni_{27}Bi_{73}$. The necessity of managing the trade-off between energy cost and activity in the catalyst optimization by means of carefully screening metal alloys therefore emerged as a crucial component of reactor design. In subsequent years, several valuable investigations were conducted to achieve this objective. Palmer et al.[36] discovered that while neither Cu nor Bi is a good catalyst, molten $Cu_{45}Bi_{55}$ alloy showed a slightly higher methane conversion than $Ni_{27}Bi_{73}$. Zeng et al.[37] investigated Te vapor as well as NiTe and Te molten metals in a bubble column reactor and reported the interesting finding that molten Te has the lowest activation barrier toward methane pyrolysis. Zaghloul et al. compared Sn, SnCu, and SnNi molten metals and found that the addition of Ni and Cu improved the rate constants though the activation barrier increased.[38] Scheiblehner et al. investigated other binary alloys of Cu with inert metals and Ni, concluding that CuBi exhibited the best reactivity, followed by CuNi, CuSn, and CuGa.[39] Finally, Kim et al.[40] studied the NiSn molten alloy for methane pyrolysis and observed a significantly increased activity at low temperatures even with a 20% Ni alloy.

Although CH_4 pyrolysis shows promise as an emerging method for H_2 production, the successful commercialization of this process relies on, among many other factors, the careful selection of the composition of the molten metal component. This presents a significant challenge, as it entails extensive material selection with a vast search domain. From the experimental work conducted so far, it is evident that at least a bimetallic alloy would be required, with the solvent serving to lower the melting point of the active component, which has a typically higher melting point. Moreover, one can even explore the inclusion of a third species in the alloy, aiming to enhance the activity of the active metal even further. Several examples from the literature showcase the intriguing synergy exhibited by such ternary alloys.[41−43] For instance, Maluf and Assaf used a Mo promoter in a solid-phase Ni catalyst to improve its activity for methane steam reforming.[44] These alloys have been previously investigated in such diverse areas as hydrocarbon conversion,[42] dry reforming of methane,[41,43] and thermocatalytic decomposition of methane[19,45] which are similar to the reaction under consideration. Hence, the main objective of this study is to understand the effect of such a promoter on the reactivity of a Ni-based alloy within a low-melting-point solvent metal, namely Bi.

Ab initio modeling, especially density functional theory (DFT)-based calculations, has been utilized for decades as an affordable support mechanism for costly and labor-intensive experimental work.[20] Theoretical reactivity markers are routinely calculated for catalysis and used in the design of experiments.[46] While ample theoretical literature can be found on solid-phase heterogeneous catalysts for various applications,[47−51] research on molten phases of metals is still in its early stages. From a first-principles perspective, the catalytic

https://doi.org/10.1021/acsaem.3c03235
ACS Appl. Energy Mater. 2024, 7, 3220−3233

activity of materials is commonly studied using the nudged elastic band (NEB) method.[52] So far, in the limited body of literature on molten-metal-based methane pyrolysis, a similar method has been employed. The rough procedure can be summarized as follows: obtaining an amorphous "molten" surface by ab initio molecular dynamics (AIMD), adsorbing the reactants, and calculating the activation barrier by the NEB.[36,37,53,54] Alternatively, thermodynamics of the reactions is also often studied by means of calculating the Gibbs free-energy difference between the adsorbed reactants and the products.[54,55] While these studies provide great insights into the reaction mechanism, they do not take into account the effect of important dynamical factors such as the motion of the metal atoms and the vibration of the molecules. These effects are especially important at a high temperature. One exception to these methods of handling such systems is the recent experimental work by Chen et al.,[56] which includes an AIMD study, looking into the charging effect of a Mo promoter in a Ni−Bi alloy. In this study, some MD runs were conducted to understand the effect of Mo on the Ni component, especially concerning the charge redistribution. A single CH_4 dissociation simulation was also included and showed clearly the positive effect of the promoter, starting from a perfectly ordered lattice. The work that we present here differs in many respects, including the preparation of the alloys, the statistical nature, and the manner in which we develop simple descriptors to understand the complex phenomenon of liquid metal alloy catalysis. A viable alternative to AIMD is the classical molecular dynamics with reactive potentials such as REAXFF.[57] However, the transferability of the generated potentials for triple alloys becomes an issue.

In this paper, we use AIMD to compare, for the first time to our knowledge, the reactivity of two triple molten alloys, namely, NiBiCu and NiBiAl. To reach this goal, we follow a calculation scheme that is rather different from what is currently available in the literature. Following meticulous protocol determination steps, we first highlight the difficulties associated with calculating the reaction rates and barriers with conventional methods. We concentrate on and classify each dissociation event in all steps of the full pyrolysis mechanism, given by the sequence in eqs 2−5. We rationalize the global behavior of the triple alloys via detailed analysis of the local environment of the reactions and come to a concrete conclusion regarding the relative performance of the two promoters, Cu and Al. To the best of our knowledge, such a detailed investigation is the first of its kind.

This paper is organized as follows: in Section 2, we detail the methods used in our analysis. Section 3 reports our ab initio results on the rates, activation barriers, and local reaction environments and rationalization of these results. The paper concludes with Section 4, which summarizes the most important conclusions and presents an outlook for future investigations on this topic.

2. METHODS

All calculations reported in this work were performed within the density functional theory (DFT) and ab initio molecular dynamics (AIMD) frameworks as implemented in the Vienna ab initio simulation package (VASP).[58−60] Electron exchange and correlation were treated within the Perdew−Burke−Ernzerhof (PBE)[61] approximation to the exchange−correlation, while projector-augmented wave (PAW) potentials were used to model the interaction between electrons and nuclei.[62,63] The van der Waals correction was included using the DFT + D3 method by Grimme.[64] Following an extensive parameter test detailed in the Supporting Information section, a cutoff of 340 eV was observed to be sufficient for the plane-wave expansion. Brillouin zone integrations were performed at the Γ point. The AIMD calculations were carried out under the *NPT* and *NVT* ensembles, as needed, at 3000 K.

In this work, we considered the performances of four main alloy compositions: $Bi_{70}Ni_{20}Cu_{10}$, $Bi_{70}Ni_{20}Al_{10}$, $Bi_{60}Ni_{20}Cu_{20}$, and $Bi_{60}Ni_{20}Al_{20}$. Additionally, Bi−Ni binary alloys as well as pure liquid Bi and Ni were considered to form a baseline for comparison. Our analysis began with a detailed reactivity assessment of these alloys for the $CH_4 \rightarrow CH_3 + H$ reaction. Once the best protocol for determining reactivity was established, the rest of the reaction steps in the full mechanism were analyzed. Here, we outline our method of analysis for CH_4 decomposition to CH_3.

All liquid metal alloys were represented by using two different models. In the first model, for each alloy, a periodic simulation box with a total of 200 randomly distributed metal atoms with the correct constituent ratio was constructed using the PackMol software suite[65] (see Figure 1a). The high-temperature density data for molten alloys,

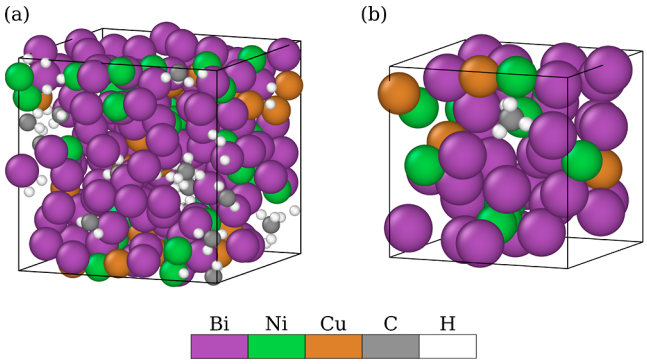

Figure 1. Large (200 metal atoms) (a) and small (50 metal atoms) (b) representative simulation boxes to model the $Ni_{70}Bi_{20}Cu_{10}$ alloys. The color codes for the atoms are also given.

especially those consisting of three components, are not readily available in the literature. Thus, an initial *NPT* calculation was performed for each alloy to accurately represent the equilibrium-specific volume and hence the density. The optimized parameters used in our *NPT* calculations are reported in detail in Tables S1−S3 of the Supporting Information. Once the supercell volume was determined, 20 randomly distributed CH_4 molecules were introduced into each simulation box, without changing the volume. A thermalization stage of 3000 steps with a step size of 1 fs was then conducted at 3000 K within the *NVT* ensemble. In this stage, the C−H bond distances in the CH_4 molecules were constrained to their equilibrium values to prevent premature dissociation. Following the thermalization stage, the production runs were initialized by removing the constraint on the bond lengths. To improve the time resolution of the dissociation events, the time step in this stage was reduced to 0.5 fs. Throughout these runs, all C−H bond lengths were monitored, and the $CH_4 \rightarrow CH_3 + H$ transition was defined as the moment where any of the C−H bonds of the CH_4 molecule exceeded 2 Å. An example can be seen in Figure S1 panel (c) where three of the C−H distances oscillate around the equilibrium value while the fourth one displays dissociation. None of the dissociated H atoms were observed to reattach to the C atom once the C−H distance exceeded this threshold. The simulations in this final stage were carried out for 10,000 steps, corresponding to a duration of 5 ps.

The rate of the $CH_4 \rightarrow CH_3 + H$ reaction was determined using the rate equation for first-order reactions

$$\ln [CH_4]_t = -kt + \ln [CH_4]_0 \quad (6)$$

where $[CH_4]_0$ and $[CH_4]_t$ refer to the undissociated CH_4 concentration at time $t = 0$ and a later time t, respectively. Here, $t = 0$ designates the start of the production runs. The reaction rate k is

https://doi.org/10.1021/acsaem.3c03235
ACS Appl. Energy Mater. 2024, 7, 3220−3233

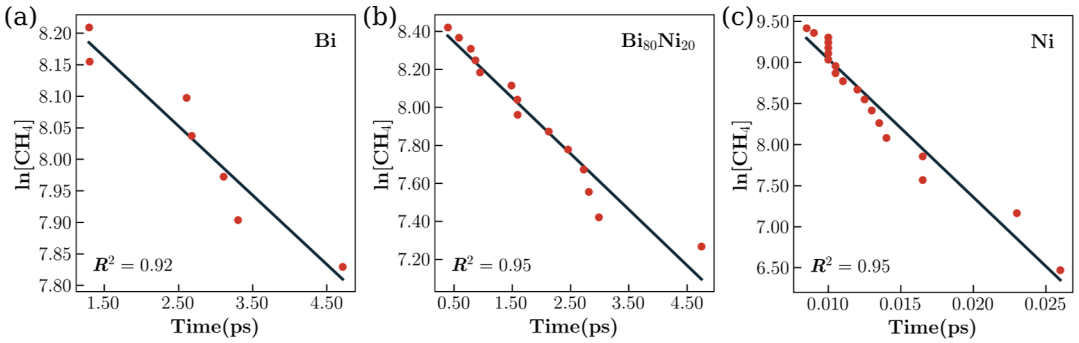

Figure 2. CH_4 dissociation rate plots for 100% Bi (a), $Bi_{80}Ni_{20}$ (b), and 100% Ni (c) liquid metal alloys. Each red dot corresponds to a dissociation event that decreases the number of CH_4 atoms by one. The solid black line corresponds to the linear fit according to eq 6. The R^2 measure was also included in the bottom left corner of each fit.

calculated via the negative slope of a linear fit to the time evolution of the number of intact CH_4 molecules per volume.

Our initial rate calculations were performed in simulation boxes with 200 metal atoms and 20 methane molecules. However, most of the remaining calculations reported in this work were performed in smaller boxes with 50 metal atoms, each containing a single CH_4 molecule (see Figure 1b). Specifically, for each alloy, 20 separate boxes with a single CH_4 were prepared instead of placing 20 CH_4 molecules in a larger box. The smaller models make it possible to isolate each dissociation event, eliminating such complications as coupling between fragments. Additionally, in the smaller models, the simulation box was randomized independently before each individual event, resulting in better statistics. Furthermore, smaller simulation boxes allow for a more efficiently parallelized and faster workflow, considering the large number of calculations involved. For each alloy composition, the smaller simulation cells with 50 metal atoms with the appropriate alloy composition and a single CH_4 molecule were prepared with the same *NPT* → *NVT* thermalization → *NVT* production sequence described earlier for the larger simulation boxes with a 1 fs time step, and the time at which the reaction occurred was recorded and collected.

To gain insights into the atomistic origins of the overall reactivity trends, we conducted a detailed analysis of each individual CH_4 dissociation event. Due to the complexity arising from the high temperature and disorder of the liquid metal, traditional transition-state identification methods like nudged elastic band (NEB)[52] are not suitable for straightforward reactivity analysis. Instead, large-amplitude molecular vibrations, collision-induced gain in velocity, and diffusion significantly complicate the reaction dynamics. Consequently, a clean definition of an activation barrier presents great difficulty. Nonetheless, we aimed to extract some form of barrier height for each C−H dissociation event through a semistatic approach. To accomplish this, we first identified each dissociation event, specifically focusing on the time interval just before dissociation occurs. To avoid a large energy background originating from the full system, we only consider the metal atoms within a neighborhood with a radius of 5 Å centered around the dissociating H atom of the CH_4 molecule at the moment the C−H bond exceeds 2.0 Å. By considering only the atoms that fall into this neighborhood, we calculate the single-point self-consistent field (SCF) energy of each of the steps bracketing the dissociation. For these SCF calculations, we used a kinetic energy cutoff of 520 eV. In almost all of the events studied, we were able to clearly identify the energy minimum and maximum. The difference between the energy minimum just before reaction and the maximum just after was identified as a "reaction barrier", as illustrated in Figure S1 panel (d) in Supporting Information. This, of course, is not a true activation barrier in the sense of the transition-state theory[66] and is only meant to give an idea about the energy cost associated with the reaction. A slightly different version of this method was previously utilized by Han et al. as an estimate[67] for barriers. In addition to the extended neighborhood defined using a cutoff of 5 Å, we repeated the SCF calculations in a much smaller, immediate neighborhood of the reaction. The atoms included in this immediate neighborhood were chosen visually on an event-by-event basis, typically consisting of around four atoms but ranging from two to six. A second set of SCF barriers was calculated for these immediate neighborhoods, allowing us to compare them with the barriers obtained from the extended neighborhoods. This comparison revealed the contribution of the environment to the reaction barrier.

Since partial charges are often considered as descriptors of reactivity,[35] we monitored the Bader partial charges on the two metal atoms closest to the carbon in CH_4 and the dissociating hydrogen (H) atom using the implementation by the Henkelman group[68] (see Figure S1 panel d). Animations of the representative individual events are included as part of the Supporting Information.

All subsequent steps of the reaction mechanism were analyzed using smaller 50-atom cells and the same calculation protocol. For example, following the first reaction, namely the dissociation of CH_4 into CH_3, the second reaction $CH_3 \rightarrow CH_2 + H$ was analyzed by randomly generating 20 entirely new 50-atom cells. Each cell was then subjected to a thermalization step, followed by the introduction of a single CH_3 fragment.

One of the objectives of this work is to gain a detailed understanding of the role played by the local environment in each reaction, with the aim of uncovering predictive patterns. To this end, the next question we address is which metals trigger reactions more often than others. In an attempt to provide an answer, we zoom in further on the metal or metals that are in direct contact with the reactant molecule before each step of the reaction and the product fragments after. The statistical data gathered in this way revealed interesting trends, all of which will be detailed in the Results and Discussion section. In particular, the synergistic proximity effects of the metals on one another have proven to be important for rationalizing our reactivity results. This means that not only is the species of the metal in direct contact with the molecules important but the immediate neighbors of that metal also play a role as well. To provide a simplified understanding of the promoting effect of the alloy components on one another, we considered diatomic clusters of all relevant combinations of these four species: NiAl, NiCu, NiBi, BiAl, and BiCu. We then investigated the adsorption characteristics of the reaction intermediates on these clusters. The formation energies of the bimetallic cluster XY (X, Y = Ni, Al, Cu, Bi) was calculated using the formula

$$E_f = E_{XY} - E_X - E_Y \tag{7}$$

where E_{XY}, E_X, and E_Y are the total energies of the geometry-optimized XY cluster, an isolated X atom, and an isolated Y atom. All energy calculations used in eq 7 were conducted at the Γ point and in a large cubic simulation box. Spin-polarization was employed. As a potential measure of reactivity, the Bader partial charges on the atoms constituting the bimetallic cluster were also calculated and are reported in the next section.

https://doi.org/10.1021/acsaem.3c03235
ACS Appl. Energy Mater. 2024, 7, 3220−3233

For each bimetallic cluster, the adsorption energies of reaction products (CH_3, CH_2, CH, C, and H) were calculated according to the formula

$$E_a = E_{XY+ads} - E_{XY} - E_{ads} \quad (8)$$

where E_{XY+ads}, E_{XY}, and E_{ads} are the total energies of the full system with the adsorbate, the cluster, and the isolated adsorbate molecule, respectively. Adsorption is considered at both the X and Y ends of each bimetallic cluster.

After a thorough evaluation of these analysis methods, for the first time to the best of the authors' knowledge, the most accurate, realistic, and cost-effective analysis method was identified to be the reaction time (i.e., time elapsed from the beginning of the *NVT* production runs and the moment the dissociation event occurs) of the single events collected in a single graph. This method presents a very affordable and fast alternative for reliably understanding the reactivity of each alloy. Armed with this analysis protocol, all the data from all the bond dissociation steps of the pyrolysis mechanism, namely $CH_3 \rightarrow CH_2 \rightarrow CH \rightarrow C + H$, were collected and will be discussed in detail in the following section.

3. RESULTS AND DISCUSSION

3.1. Rate Constant Calculations. The rate constants were initially calculated for CH_4 dissociation using the larger simulation boxes for the first step of the pyrolysis reaction mechanism $CH_4 \rightarrow CH_3 + H$. Each box contains 200 metal atoms and 20 CH_4 molecules. As a benchmark, the rates for pure Bi, $Bi_{80}Ni_{20}$, and Ni melts were also calculated. The $\ln[CH_4]$ versus time data and the corresponding linear fits are shown in Figure 2, where $[CH_4]$ is the concentration of the intact CH_4 molecules in the box. The calculated rate constants for the three liquid metals are k = 0.11 ps^{-1} for Bi, k = 0.29 ps^{-1} for $Bi_{80}Ni_{20}$, and k = 168.24 ps^{-1} for Ni, respectively. These results are in line with expectations, where the rate constant of pure Ni is approximately 3 orders of magnitude higher than that of pure Bi, and the alloy performs twice as well as pure Bi. These findings serve as a baseline for comparing the rates of other alloys, demonstrating the consistency of our protocol.

Next, we explore the rates of the main Ni-based double and triple alloys that are the focus of this work. To ensure fair comparison, we examine systems with an equal percentage (20%) of Ni atoms. Additionally, we attempt to quantify the effect of the promoter (Cu or Al) amount by considering three different promoter percentages, namely, 0, 10, and 20%. To establish a baseline for the Cu- and Al-promoted alloys, we also include 20 and 30% Ni-loaded Bi−Ni alloys in our data set. The rates reported for all of these alloys were calculated using the same protocol as described earlier, employing the large simulation cells. Table 1 presents the rates for the six alloys: $Bi_{80}Ni_{20}$, $Bi_{70}Ni_{30}$, $Bi_{70}Ni_{20}Cu_{10}$, $Bi_{60}Ni_{20}Cu_{20}$, $Bi_{70}Ni_{20}Al_{10}$, and $Bi_{60}Ni_{20}Al_{20}$. Scatter plots of $\ln[CH_4]$ versus time and the corresponding fits are provided in Figure S2 of the Supporting Information. For the two Ni−Bi alloys considered, increasing the percentage of Ni clearly increases the rate. Replacing some of the Bi atoms with the Al and Cu promoters for the same number of Ni atoms also improves the reaction rate in comparison to the Bi−Ni double alloys. Moreover, increasing the percentage of the same promoter also resulted in a higher rate. However, the relative effect of the two promoters, when compared at the same percentage, is less conclusive as the rates obtained for both $Bi_{70}Ni_{20}X_{10}$ (X = Al, Cu) and $Bi_{60}Ni_{20}X_{20}$ (X = Al, Cu) appear to be too close for declaring a clear superior promoter.

Table 1. Reaction Rates for Various Double and Triple Alloy Compositions

alloy	k [ps^{-1}]
$Bi_{80}Ni_{20}$	0.29
$Bi_{70}Ni_{30}$	0.38
$Bi_{70}Ni_{20}Cu_{10}$	0.49
$Bi_{60}Ni_{20}Cu_{20}$	0.86
$Bi_{70}Ni_{20}Al_{10}$	0.47
$Bi_{60}Ni_{20}Al_{20}$	0.71

Considering the similar rates obtained for the two promoters, as well as the presence of scatter and outliers in the data, as seen in Figures 2 and S2, conducting a more detailed comparison of the dissociation will be helpful. Therefore, instead of applying a fit, we opt for a visual comparison of the dissociation times defined as the moment in time when one of the C−H bonds in a CH_4 molecule reaches 2 Å. Here, t = 0 marks the beginning of the production run after the volume adjustments and thermalization stages are completed. Figure 3 displays the times of all the $CH_4 \rightarrow CH_3 + H$ dissociation events for the four alloy compositions with the promoters. Table S4 presents the statistics of the dissociation times for all four alloys. These qualitative findings suggest that Cu exhibits a slightly higher activity compared to Al for both promoter percentages, as implied also by the fits.

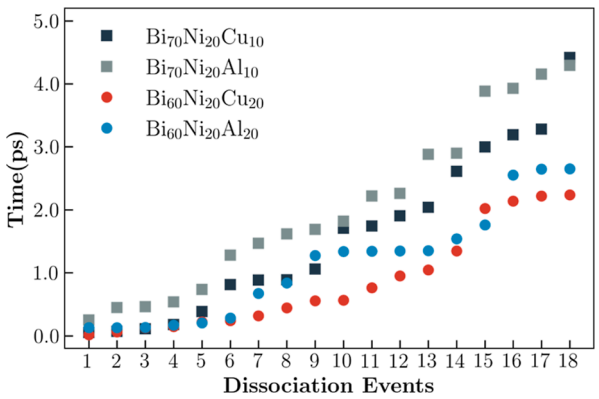

Figure 3. Hydrogen dissociation times for the $CH_4 \rightarrow CH_3 + H$ reaction calculated in the larger simulation cells for the four ternary alloys.

The increase in rates resulting from the incorporation of the third component in the metal melt may be due to two main effects. The promoter atoms might directly participate in the dissociation reaction, actively contributing to the overall reactivity. Alternatively, they could have an indirect effect on the Ni atoms through such mechanisms as charge transfer.[69] Previous studies have reported that both Cu[43] and Al[70] have some reactivity toward C−H bond scission. This could explain the higher rates observed for the triple alloys that have 20% promoter compared to those with 10% promoter. However, the even higher rates observed for the triple alloys with 10% Al or Cu, in comparison to $Bi_{70}Cu_{30}$, are likely due to a synergistic effect, where the promoter may indirectly increase the activity of the Ni component.

To gain a comprehensive understanding of the possible mechanisms and subtleties behind these global results, we shift our focus to analyzing individual dissociation events. We first provide a detailed account of CH_4 dissociation to CH_3,

https://doi.org/10.1021/acsaem.3c03235
ACS Appl. Energy Mater. 2024, 7, 3220−3233

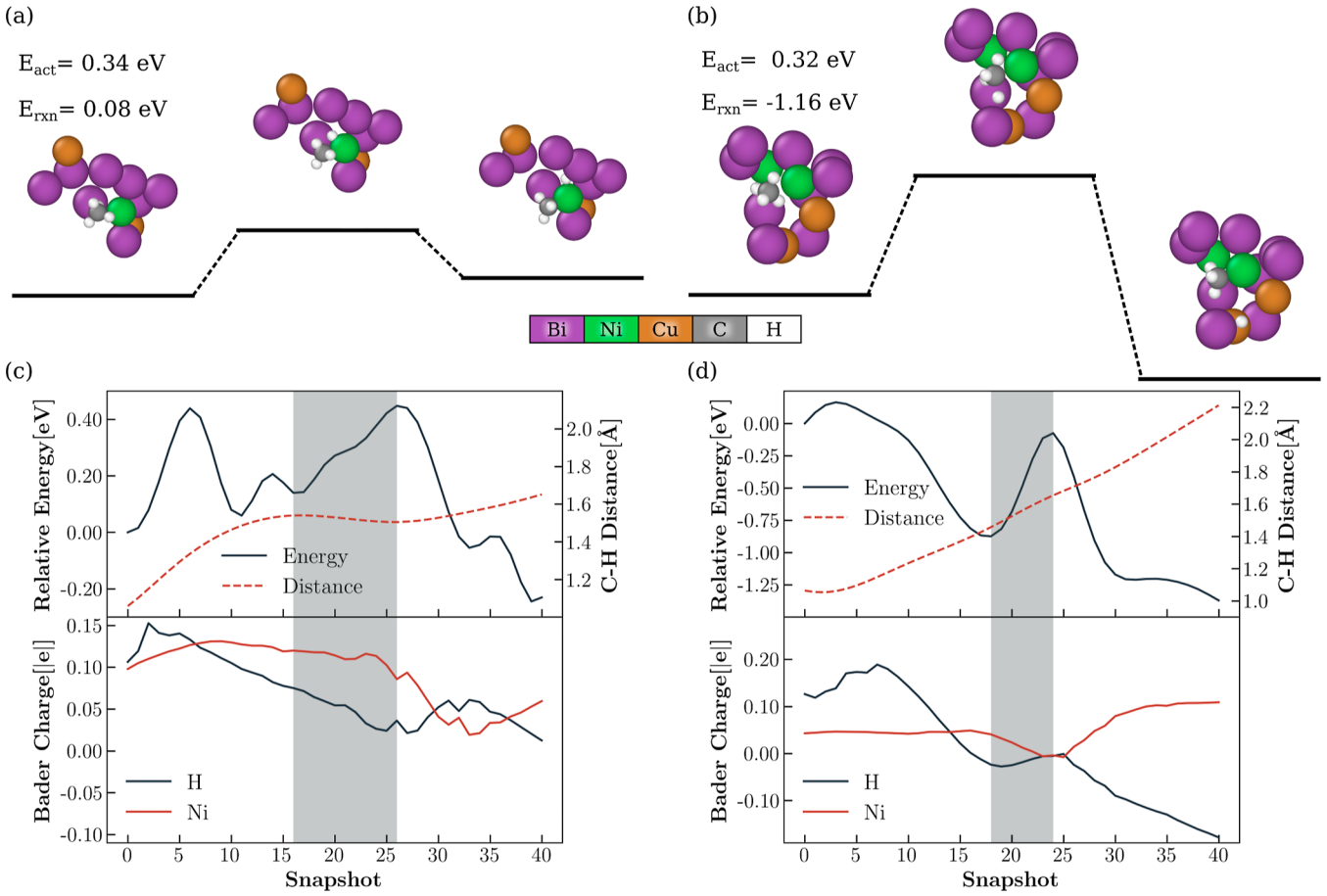

Figure 4. Nudged elastic bands (a,b) and SCF reaction barrier (c,d) calculations for the same two reactions. The color-coding of the atoms is as seen on the central color bar. The SCF panels are divided into two parts where the top plot is the total energy of the molecule and the surrounding metals and the C−H bond between the central C atom and the dissociating H. In the lower panel, the Bader charges of the dissociating H and the Ni atom (green) nearby are shown. The gray band represents the dissociation event as delimited by the energy minimum and maximum.

followed by more concise results on the complete reaction mechanism.

3.2. Analysis of Individual Dissociation Events. As described in the Methods section, in our AIMD simulations, a CH_4 molecule was considered dissociated once any of the C−H distances reached 2 Å. This point in time was recorded as the dissociation time for the specific reaction event. All dissociation times were then recorded for a given alloy and analyzed. Dissociation times calculated for a single large cell and for the 20 smaller cells are compared in Figure S3. The results do not display any serious discrepancies, validating our method based on smaller cells.

To gain insights into the atomistic mechanisms governing the reaction times, each isolated dissociation event was analyzed in detail. In contrast to static reaction barrier calculations on ordered surfaces performed with methods such as NEB, the molten method environment presents unique challenges. To begin with, monitoring the total energy of the full system during the reaction becomes impractical due to the dynamic motion of reactants, products, and surrounding metal atoms that change positions throughout the process. Additionally, a static reaction calculation ignores molecular vibrations, which becomes more important at higher temperatures.[71] In fact, animations of our reactions included in the Supporting Information clearly show that the reactions are triggered by molecular vibrations. To address these challenges, we extract some form of a reaction barrier via a series of SCF calculations of each frame around each dissociation event, as described in the Methods section. Figure 4 is a comparison of the NEB and SCF reaction barriers for the same events. The total energy in all dissociation events is reported relative to the very first image of each plot.

The NEB and SCF calculations presented here not only yield different energy barriers but also result in different reaction paths. The initial and final configurations for the NEB calculations do not correspond to local minima since both are taken from snapshots during the simulation and are not obtained as a result of geometry optimization. Therefore, the trajectory of the metal atoms is not realistic. Nevertheless, it is noteworthy that the activation barrier for the Ni atom in the disordered system is significantly smaller than that on ordered Ni(111)[72] and Ni clusters[73] reported in the literature. Figure 5 illustrates some examples of dissociation events and the associated energy barriers. Additionally, full animations of these dissociation events are also provided in the Supporting Information.

To understand the influence of the neighborhood size considered in the single-point energies, we conducted two sets of SCF energy barrier calculations. In the first set, we included all metal atoms within a radius of 5 Å. In the second set, we included only immediate neighbors of the atoms on which the reaction occurs, as described in the Methods section. The

https://doi.org/10.1021/acsaem.3c03235
ACS Appl. Energy Mater. 2024, 7, 3220−3233

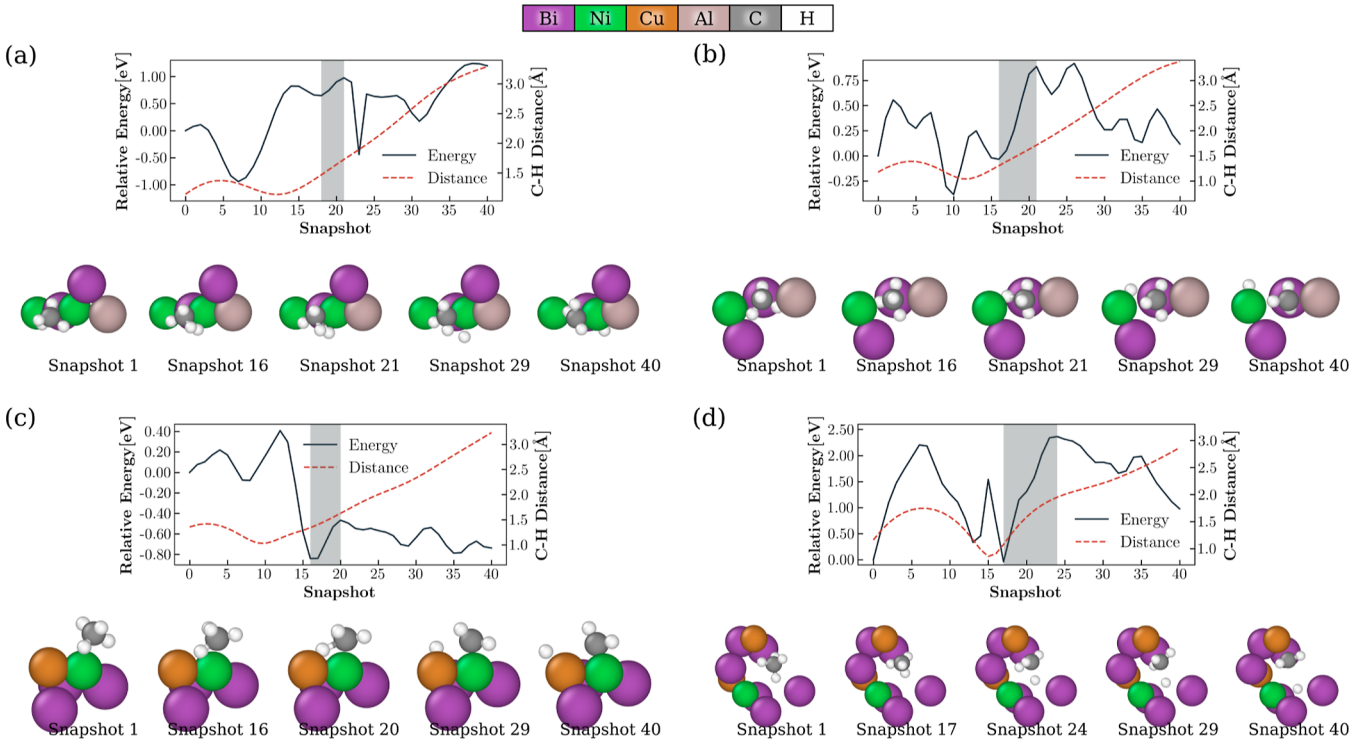

Figure 5. Four different types of dissociation events with total energy (solid black lines) and C−H distance (dashed red lines) plots: an event where CH_4 dissociation on top of a single Ni (a), around a Ni and a Bi (b), around a Ni and a Cu (c), and with the contribution of several atoms (d). For each event, five snapshots are shown chosen among the 40 snapshots that define the gray dissociation regions. The color codes of the atoms are shown in the top color bar.

energy barriers calculated for all events in the four alloy compositions using both the smaller and the larger set of nearby atoms are presented with bar charts in Figure 6, and a statistical analysis of these results is provided in Table 2. In several instances, the barriers calculated for the reactions using the immediate neighborhoods are higher than those for the extended neighborhoods. However, despite the absolute values of the barriers differing by as much as 100% or more in the two sets of calculations, the general trends remain roughly the same. The activation energies represented by the bar charts reported in Figure 6 are ordered with respect to their time of dissociation. In other words, the smaller the event number the earlier is the associated dissociation. There does not appear to be any correlation between the barrier and the dissociation time.

Next, we consider the precise dynamics of each event to gain a microscopic understanding. Upon careful observation, the diversity in the types of reactions involved becomes evident. Although numerous events exhibit a wide range of reaction paths, most of them can be categorized into four main classes. Examples of each class, along with snapshots and the corresponding energy profiles, are depicted in Figure 5. The first class involves the complete dissociation of a CH_4 molecule on a single metal atom. In this scenario, the CH_4 molecule approaches a metal atom, the H atom breaks, and the product fragments CH_3 and H remain attached to the same metal atom. Figure 5a illustrates an example of this class of reactions. While Ni is the primary metal atom involved in most events of this class, other elements are also seen to initiate such reaction paths. In the second type of dissociation events, exemplified in Figure 5b, the reaction products CH_3 and H remain attached to two neighboring atoms throughout the reaction. The reaction shown in Figure 5c is similar to that in Figure 5b except that the reaction starts on one metal, and then the dissociating H moves on to a neighboring atom. The reaction shown in Figure 5d, on the other hand, follows a peculiar path in which the H atom is, in a sense, propelled into the void between several atoms. The lower reaction barrier associated with Figure 5a−c in comparison to that of Figure 5d can be due to the fact that the first three are assisted by neighboring atoms, while the latter is not assisted from the H side.

An important conclusion that has been reached based on our analyses so far is the following: activation barriers, in addition to being difficult to define and compute, cannot be considered reliable indicators of relative reactivity for disordered systems at high temperatures. Unlike their crystalline counterparts, reactions in disordered systems exhibit substantial diversity, with various confounding factors such as energy gained via recoil, diffusion, molecular vibrations, and the displacement of metal atoms during reactions. Conversely, relying solely on the rate, which is a single value obtained from fitting data with scatter, can be misleading, especially for systems with rates that are on the same order of magnitude. However, the dissociation times have so far persistently given reliable results for both the small and the larger simulation boxes. We therefore continue our analysis of the rest of the reaction mechanism using only dissociation times. In the next subsection, we report on the full mechanism and attempt to understand the trends by means of zooming in on the local environments of each of the dissociation events.

3.3. Full Mechanism and the Effect of the Local Environment. In Figure 7, we present the sorted C−H bond dissociation times for all reaction steps and alloys considered. The mean dissociation times are shown in Figure 8 and listed

https://doi.org/10.1021/acsaem.3c03235
ACS Appl. Energy Mater. 2024, 7, 3220−3233

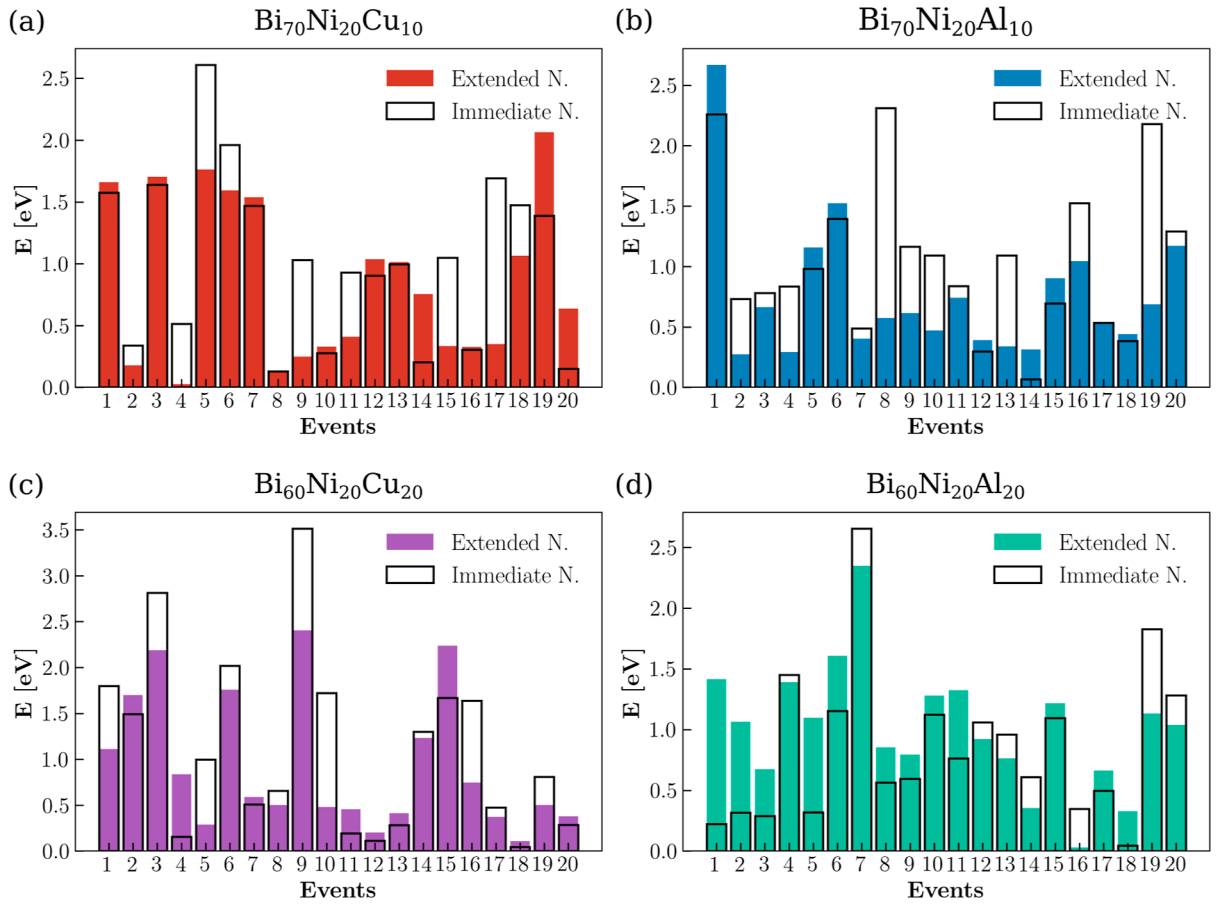

Figure 6. Bar chart representation of all events studied in small systems for $Bi_{70}Ni_{20}Cu_{10}$ (a), $Bi_{70}Ni_{20}Al_{10}$ (b), $Bi_{60}Ni_{20}Cu_{20}$ (c), and $Bi_{60}Ni_{20}Al_{20}$ (d). The colored bars correspond to activation barriers computed for neighbors within the 5 Å radius of the dissociating hydrogen while empty bars represent the barriers involving only the immediate neighbors. The events are sorted according to reaction times, with the leftmost event in the bar chart being the earliest to occur.

Table 2. Average ($\bar{E}$), the Median, and the Standard Deviation (σE) in eV of the Activation Barriers of All Dissociation Events (for the $CH_4 \rightarrow CH_3 + H$ Reaction) for All the Compositions Considered in This Work

	extended neighborhood			immediate neighborhood		
	$\bar{E}$ [eV]	median (E) [eV]	σ_E [eV]	$\bar{E}$ [eV]	median (E) [eV]	σ_E [eV]
$Bi_{70}Ni_{20}Cu_{10}$	0.8583	0.6969	0.6382	1.0318	1.0133	0.6753
$Bi_{70}Ni_{20}Al_{10}$	0.7546	0.5946	0.5540	1.0467	0.9091	0.6204
$Bi_{60}Ni_{20}Cu_{20}$	0.9262	0.5471	0.7183	1.1243	0.9022	0.9337
$Bi_{60}Ni_{20}Al_{20}$	1.0148	1.0514	0.4963	0.8587	0.6859	0.6142

in Table 3. The full statistical analyses of the mean dissociation times including the median and the standard deviation can be found in Tables S5−S8 in the Supporting Information. These results reveal several interesting trends that we will discuss in some detail here.

The bottleneck reaction for both the 10% Cu and 10% Al alloys is the first H dissociation, i.e., $CH_4 \rightarrow CH_3 + H$, while for the 20% alloys, it is the second ($CH_3 \rightarrow CH_2 + H$). Additionally, increasing the promoter percentage from 10 to 20% causes a sizable (≈50%) decrease in the mean reaction time for the first step. It is worth noting that a decrease of this size is not observed for any of the subsequent reaction steps. In contrast, all alloys perform very similarly for CH_3 dissociation, i.e., the second step. Interestingly, for the second step, both 10% alloys perform slightly better than the 20% ones, although we do not attribute much statistical meaning to this observation due to the very close values. Regarding the final two steps of the mechanism, the order of performance is less predictable. However, overall, with the marginal exception of the second step, $Bi_{60}Ni_{20}Cu_{20}$ clearly outperforms all other alloys.

As mentioned earlier, the effect of the promoters could be twofold: direct and indirect. Furthermore, due to the overwhelmingly large number of Bi atoms, it is possible to observe a non-negligible number of reactions on the Bi atom, as well. To understand the effect of the local environment on the reactivity, we conducted a detailed mapping of the metal species that were nearest to the C and H atoms as well as the nearest metal to the neighbor, at the time of the dissociation event. Specifically, the nearest metal (NM) was defined to be the closest atom to either the C atom or the H atom at the time of dissociation. The next nearest metal (NNM), on the other hand, was defined to be the metal atom closest to the NM at the same moment. Thus, for each dissociation event, we

https://doi.org/10.1021/acsaem.3c03235
ACS Appl. Energy Mater. 2024, 7, 3220−3233

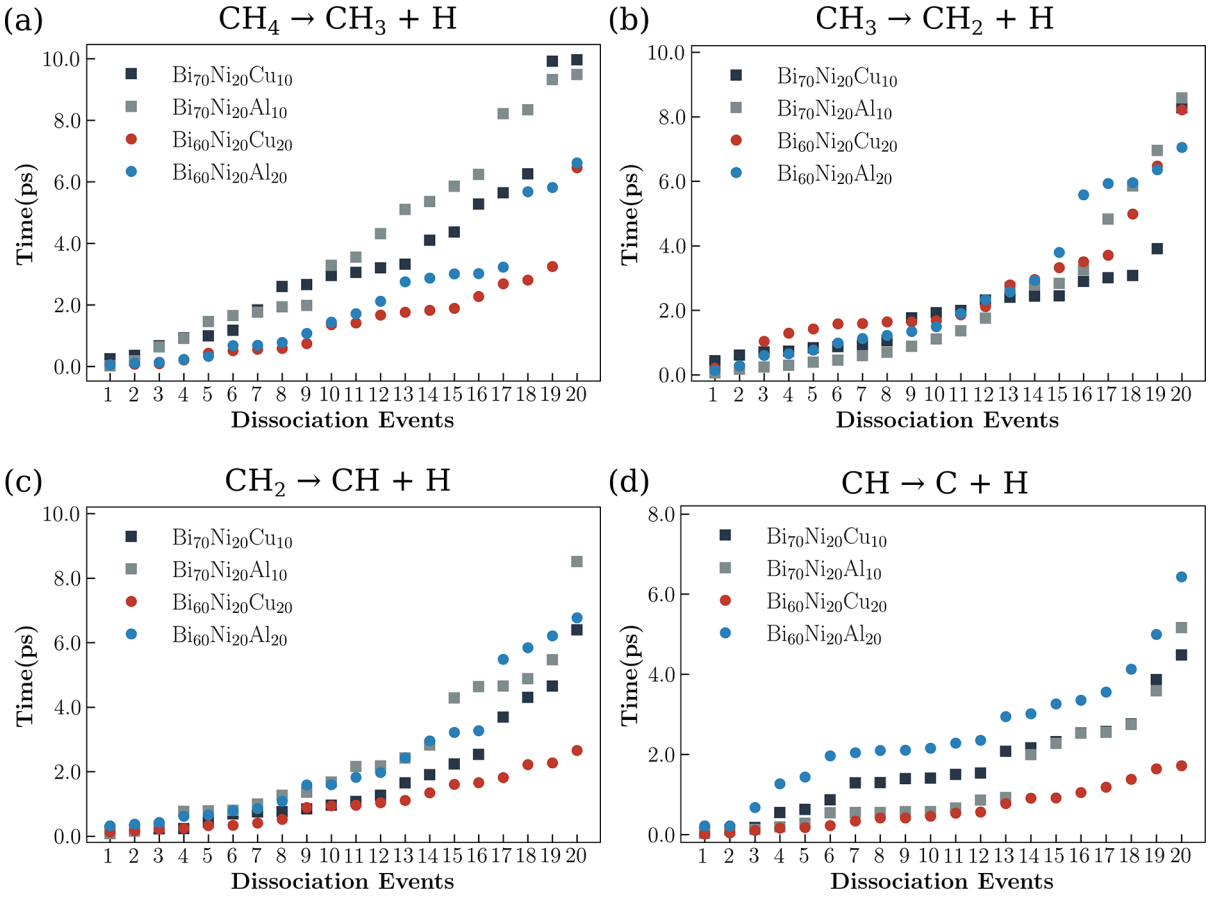

Figure 7. Reaction times for all methane pyrolysis steps and alloys: $CH_4 \rightarrow CH_3 + H$ (a), $CH_3 \rightarrow CH_2 + H$ (b), $CH_2 \rightarrow CH + H$ (c), and $CH \rightarrow C + H$ (d). The events labeled on the horizontal axes are sorted in ascending dissociation time.

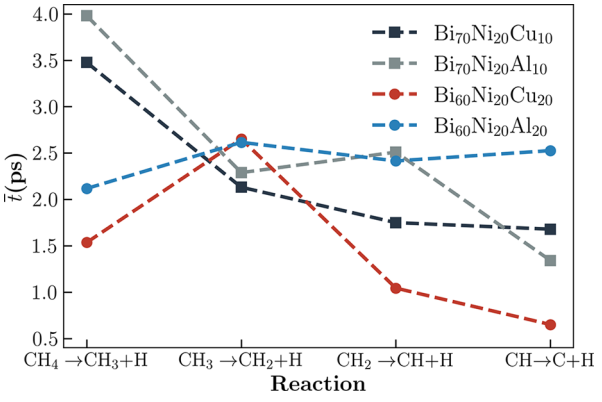

Figure 8. Mean hydrogen dissociation times for all methane pyrolysis steps and all alloys investigated in this work.

collected four pieces of neighbor information: NM for C, NM for H, NNM for C, and NNM for H. This data set is consolidated in the form of donut charts in Figure 9 for CH_4 dissociation and Figures S4−S7 for all other reaction steps. A comprehensive list of all NM and NNM for all events in all four reaction steps can be found in Tables S9−S12. Once again, the events in these tables are sorted with respect to their dissociation times. The NM data are interpreted as a predictor of the direct effect of a metal, while the NNM represents the secondary promoting effect. These charts reveal many interesting properties of the reaction environments and their correlations with the reaction times. To further elucidate some of the observed behaviors, we analyzed the formation energies of the bimetallic clusters and Bader charges on the metal atoms in these clusters. These results are provided in Table 4. Additionally, the fragment adsorption energies to these bimetallic clusters are given in Table 5, and the adsorption geometries are displayed in Figures S7−S8 of the Supporting Information. During the compilation of these results, we ensured that the same adsorption geometry was used for each adsorbate across different clusters. These analyses are meant to

Table 3. Mean Dissociation Time for All Reaction Steps and All Triple Alloys[a]

reaction step	$Bi_{70}Ni_{20}Cu_{10}$	$Bi_{70}Ni_{20}Al_{10}$	$Bi_{60}Ni_{20}Cu_{20}$	$Bi_{60}Ni_{20}Al_{20}$
$CH_4 \rightarrow CH_3 + H$	**3.4759**	**3.9793**	1.5358	2.1179
$CH_3 \rightarrow CH_2 + H$	2.1312	2.2890	**2.6154**	**2.6519**
$CH_2 \rightarrow CH + H$	1.7499	2.5096	1.0437	2.4149
$CH \rightarrow C + H$	1.6792	1.3418	0.6512	2.5265

[a]The bottleneck reaction is indicated in boldface for each alloy.

https://doi.org/10.1021/acsaem.3c03235
ACS Appl. Energy Mater. 2024, 7, 3220−3233

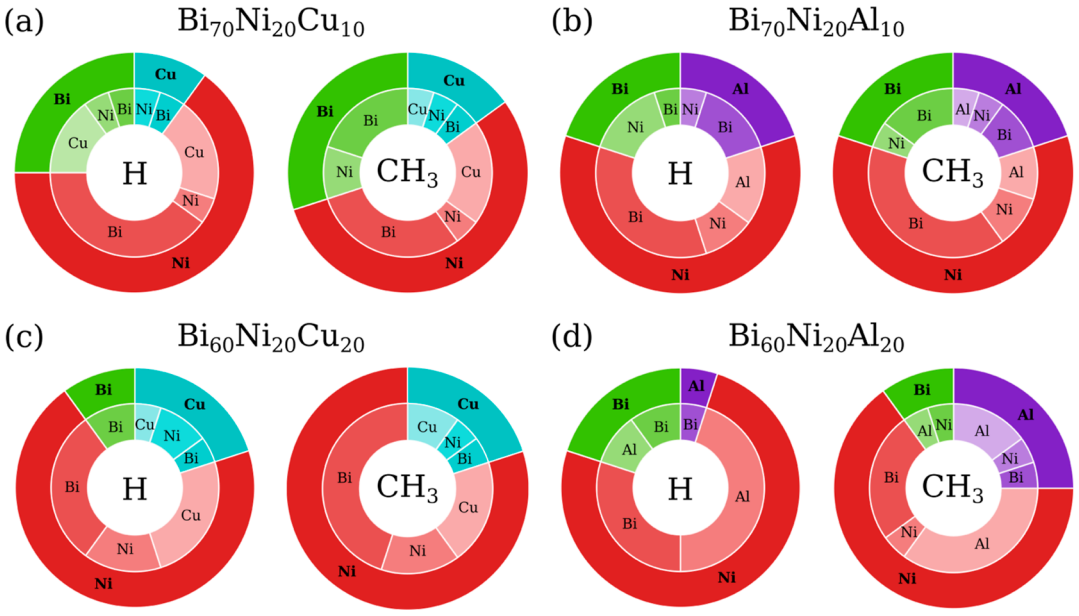

Figure 9. Donut charts illustrating the percentages of the NM and the NNM of all events during the $CH_4 \rightarrow CH_3 + H$ elementary dissociation step (see text for the definition of nearest and next nearest metal) for each of the four alloys, $Bi_{70}Ni_{20}Cu_{10}$ (a), $Bi_{70}Ni_{20}Al_{10}$ (b), $Bi_{60}Ni_{20}Cu_{20}$ (c), and $Bi_{60}Ni_{20}Al_{20}$ (d). The color coding is given in the figure. The outermost ring in each donut chart is proportional to the number of reactions occurring on the particular metal atom represented by its color. The inner segments under each outer segment is the number of second nearest neighbors.

Table 4. Formation Energies and Bader Charges of the Isolated Binary Metal Alloys XY, Where X and Y Represent the Atom Species in the Alloys, Respectively

	NiBi	NiAl	NiCu	BiCu	BiAl
E_{form} [eV]	−2.8037	−3.2247	−2.6553	−2.2339	−1.9427
Bader X [$|e|$]	−0.1336	−0.6651	0.0566	0.0941	−0.4149
Bader Y [$|e|$]	0.1336	0.6651	−0.0566	−0.0941	0.4149

provide insights into the roles of different metals in the catalytic process and their interactions with the reaction intermediates.

In a bubble column reactor, a majority of the reactions occur at the bubble interface. Since the bubbles thoroughly mix the alloy as they rise,[74] the fraction of Ni and Bi atoms at the interface is expected to represent their respective percentages in the alloy with an abundance of Bi atoms interacting with the gas molecules. In spite of this, at first glance, it is immediately clear from the donut charts in Figures 9 and S4−S6 that the metal atom that triggers the overwhelming majority of the dissociation events for all reaction steps is Ni. Given its small percentage, this observation reveals, without any doubt, that the Ni atoms are indeed the active components of the molten alloys. However, the actual percentage of Ni as NM varies across different reactions. For instance, while in the CH_4 dissociation step, 11 of the product CH_3 molecules have Ni as their NM at the time of the reaction for the $Bi_{70}Ni_{20}Cu_{10}$ alloy, for the same alloy in the third step, 19 of the 20 CH products were found to be near Ni atoms at the time of their dissociation. This observation correlates with the fact that the CH adsorption energies on Ni in all of the bimetallic clusters reported in Table 5 are significantly higher than those of CH_3. As a final remark on the adsorption energies, we point out that the interaction of the promoter side of the NiCu, BiCu, NiAl, and BiAl clusters with the C atom is smaller than that of the Ni or Bi side. However, Al interacts somewhat more strongly with respect to Cu. This could be an indication of the formation of aluminum carbide, which should be considered in an experimental setting.[75]

Regarding the direct versus indirect effect of the promoter, our results provide evidence for both cases. As expected, an increase in the percentage of the promoter leads to a higher

Table 5. Adsorption Energies of H, CH_3, CH_2, CH, and C on Isolated Binary Alloys

NiBi		NiAl		NiCu		BiCu		BiAl	
Ni−H	−1.5368	Ni−H	−1.9234	Ni−H	−2.0769	Bi−H	−0.8151	Bi−H	−2.0429
Bi−H	−0.9944	Al−H	−2.7669	Cu−H	−1.8835	Cu−H	−1.5626	Al−H	−2.9297
Ni−CH_3	−1.5334	Ni−CH_3	−1.8954	Ni−CH_3	−1.9578	Bi−CH_3	−0.5749	Bi−CH_3	−1.7569
Bi−CH_3	−0.6930	Al−CH_3	−2.7983	Cu−CH_3	−1.7585	Cu−CH_3	−1.4755	Al−CH_3	−2.9653
Ni−CH_2	−2.7290	Ni−CH_2	−2.5841	Ni−CH_2	−3.1653	Bi−CH_2	−1.6540	Bi−CH_2	−2.8618
Bi−CH_2	−1.9587	Al−CH_2	−3.5548	Cu−CH_2	−2.5444	Cu−CH_2	−2.2720	Al−CH_2	−3.7519
Ni−CH	−4.1003	Ni−CH	−3.6144	Ni−CH	−4.4431	Bi−CH	−2.8383	Bi−CH	−3.3842
Bi−CH	−2.6389	Al−CH	−3.9919	Cu−CH	−3.1089	Cu−CH	−2.8767	Al−CH	−4.1020
Ni−C	−3.8908	Ni−C	−3.5574	Ni−C	−4.3128	Bi−C	−3.0885	Bi−C	−3.8530
Bi−C	−2.9936	Al−C	−3.2156	Cu−C	−2.4646	Cu−C	−2.3393	Al−C	−2.6881

https://doi.org/10.1021/acsaem.3c03235
ACS Appl. Energy Mater. 2024, 7, 3220−3233

number of Al or Cu atoms as NMs for all reactions. In other words, as the availability of the promoter atoms increases, the direct dissociation reactions that occur on these atoms also increase. However, interestingly, certain reactions appear to prefer the promoter atoms more frequently than would be suggested by their percentage. For instance, in the case of the $Bi_{60}Ni_{20}Al_{20}$ alloy, the direct contribution of Al atoms in the decomposition of CH_3 is approximately as significant as that of Ni (see Figure S4d). Specifically, the CH_2 fragment is statistically as likely to be found around Al as it is around Ni at the time of dissociation. A similar observation can be made for the next step, namely, the dissociation of CH_2.

Additionally, there is evidence of the indirect effect of the promoter in our findings, as well. The most unambiguous manifestation of this secondary effect of the promoter atom can be seen in the disproportionately large number of Al atoms as the NNM to the Ni atoms in the Al-containing alloys. This is particularly evident for the alloys with a 20% promoter. The preference of the Ni atoms to be close to Al atoms could be noticed by the large formation energy of the NiAl bimetallic cluster reported in Table 4. In fact, of all the bimetallic clusters considered, NiAl has the largest formation energy, with the second largest (NiCu) having a formation energy that is about 0.6 eV lower in magnitude. The formation energies of the NiBi and NiCu clusters are similar, which is consistent with the NNM distribution.

As another indicator of reactivity, we next consider Bader charges. As observed in the Bader charge plots in the animations of the Supporting Information, in most of the dissociation events that occur when Ni is an NM atom, there is a distinct exchange of charge between the dissociated H and the Ni atom. Ni typically starts with a negative partial charge of magnitude approximately 0.1 $|e|$, while, as expected, the charge on the H atom is initially about +0.1 $|e|$. The negative charge on Ni is expected since, upon analysis, we find that Bi atoms are positively charged. There is then a charge transfer from Bi to Ni. Throughout the dissociation event, a gradual charge exchange between Ni and dissociating H is observed. In contrast, the Bi atoms generally display slight positive charges except for the BiAl cluster (Table 4). As one might expect, the NiAl cluster, having the superior formation energy, exhibits large charge transfer between the atoms. This extra charge on the metal may facilitate the C−H bond scission,[76] which could explain the improvement in CH_4 dissociation times when the promoter percentages are doubled. In the NiCu cluster, on the other hand, Ni is almost neutral though BiNiCu shows dominance in both the rate constants and the mean dissociation times.

The comprehensive analysis of NM and NNM discussed above provides valuable insights into the reaction mechanisms taking place in the liquid alloys. However, it is essential to acknowledge that dissociation events occur within intricate environments, where each metal is surrounded by several others. Although the nearest neighbors play a significant role in explaining the observed behavior, the influence of the larger local environment cannot be overlooked.

Our final observation about the higher reactivity of the 20% Cu alloy in comparison to the others has to do with the relative ease of diffusion of the reactant molecules in different alloys. The reaction time plots displayed in Figure 7 reveal another interesting trend in this context. In the first, third, and final steps of the full pyrolysis mechanism shown in Figure 7a,c,d, respectively, long-dissociation-time or late events are observed for all alloys. Here, a late event refers to a dissociation reaction that occurs significantly later than the others, leading to the characteristic upward curve at the tail end of the plots. However, in all three plots, an exception to this trend is the $Bi_{60}Ni_{20}Cu_{20}$ alloy, where virtually no late events are present. It remains true that even for earlier events, this alloy still performs better than the others, as explained earlier. Nevertheless, the absence of these outlier events significantly reduces the mean time. The facility with which the reactions are concluded for this particular alloy suggests that it could offer a low diffusion coefficient to the molecular fragments so that molecules encounter the Ni atom that will split them earlier in the simulations. The only exception to this is the dissociation of CH_3 shown in Figure 7b. For this reaction, not only is the performance of all alloys similar for the earlier events, but all of them display a certain number of events that take place later as well. A detailed investigation into this behavior will also be explored in future studies.

4. CONCLUSIONS AND OUTLOOK

In this paper, we conducted a comprehensive ab initio analysis of ternary molten alloys, Ni−Bi−Al and Ni−Bi−Cu, to investigate their potential for CO_2-free methane pyrolysis. Due to the high temperatures involved and the inherent disorder in the molten metals, understanding the atomistic mechanisms involved in these systems is notoriously difficult. Our work achieves several important objectives. To the best of the authors' knowledge, a full reaction mechanism of CH_4 dissociations has never been investigated with this level of detail previously. We demonstrate that the results of static minimum energy path calculations do not yield results that are representative of actual reactions in such a complex environment at such elevated temperatures. In addition, in this work, we present results condensed from hundreds of reactions, each of which has been studied in detail. This in-depth investigation has revealed the rich variety of possible reactions, all with different activation barriers, as well as the crucial effect of the immediate environment (both nearest and next nearest neighbor atoms). Finally, as a practical application, our work evaluates the relative success of Al and Cu with respect to one another as promoters. Our results indicate that Cu consistently outperforms Al with a slight but discernible margin.

To summarize the details of our investigation, we began by studying the initial reaction step in the pyrolysis mechanism, which involves the dissociation of CH_4 to CH_3 with the release of an H atom. We performed AIMD calculations for four different alloy compositions: $Bi_{70}Ni_{20}Al_{10}$, $Bi_{70}Ni_{20}Cu_{10}$, $Bi_{60}Ni_{20}Al_{20}$, and $Bi_{60}Ni_{20}Cu_{20}$. While increasing the percentage of the promoter resulted in increased reaction rates, comparing the two promoters directly proved to be inconclusive due to the susceptibility of rate fits to scatter. To address this issue, we employed dissociation time graphs for comparison, which provided aclear evidence that Cu outperformed Al at both 10 and 20% levels.

Next, activation barriers for each dissociation event were computed by generating DFT single-point energy profiles around the time of the occurrence of the reaction. We explored the impact of considering a larger metallic neighborhood versus a smaller metallic neighborhood for calculating the single-point energies, and it was found that this choice had a significant effect on the results. An "activation barrier" was defined in these SCF calculations as the difference between the energy minimum and the maximum associated seen around the

https://doi.org/10.1021/acsaem.3c03235
ACS Appl. Energy Mater. 2024, 7, 3220−3233

C−H bond dissociation. The activation barriers showed great variation and revealed little to no trend. As a result, a statistical analysis of the reaction barriers obtained through this approach, while instructive, provided no definitive conclusions regarding the relative activities of the different alloys. However, this analysis was very valuable in revealing the wide range of reactions and highlighting the limitations of conventional static nudged elastic band calculations commonly employed in the literature for reactions occurring in disordered environments. The complexity of the reactions and the involvement of multiple factors make such traditional approaches inadequate in capturing the full picture.

Having settled on the mean dissociation times as a reliable and reproducible indicator of activity, we simulated the full reaction mechanism, excluding the formation of H_2 from free H atoms. These results provide conclusive predictions that hold significant value for materials design in liquid metal reactors. Overall, Cu was shown conclusively to perform better than Al in the molten alloys. In a further atomistic-scale analysis, we mapped the metal atoms responsible for triggering each dissociation event at every reaction step along with their immediate neighbors. As expected, despite its small concentration, Ni was found to directly catalyze the overwhelming majority of the dissociation events. In addition to this overarching theme, more subtle observations were made. While Al was seen to have a rather unexpected and prominent role in the direct catalysis of the reactions with respect to Cu, both promoters were also seen to have an indirect effect on the performance of Ni via charge transfer. The trends observed here were further rationalized using a simplified model of isolated bimetallic clusters and the interaction of the reaction fragments with these clusters. Results from the cluster studies were found to correlate consistently with the dissociation times.

The experience and findings gained from this work provide a strong foundation for future studies of ab initio reactivity analysis of molten alloys. The tools developed in this study can serve as a valuable framework for investigating a wide range of other promoters in molten alloys. The forthcoming studies will focus on testing and optimizing various promoters for practical use in experiments.

To expand the scope of research, constrained dynamics will be employed to simulate reactions at lower temperatures, allowing for a better understanding of the reactivity under different conditions. Additionally, machine-learning-assisted techniques will be integrated into the analysis to enhance predictive capabilities and facilitate the exploration of new alloy compositions and reaction mechanisms.

■ ASSOCIATED CONTENT

Supporting Information

The Supporting Information is available free of charge at https://pubs.acs.org/doi/10.1021/acsaem.3c03235.

Details of the *NPT* protocol used in the ab initio molecular dynamics calculations; description of how H dissociation events are monitored; reaction rate fits for six different alloy compositions for the reaction $CH_4 \rightarrow CH_3 + H$; comparison of dissociation times for the reaction $CH_4 \rightarrow CH_3 + H$ calculated by using many small simulation cells with a single initial CH_4 molecule versus many initial CH_4 molecules in a larger simulation cell; statistical analysis of mean dissociation times; individual analysis of all detachment events for all alloys and all reaction steps; and adsorption geometries of reaction fragments on bimetallic clusters (PDF)

Animation depicting an event of CH_4 dissociation on top of a single Ni (MP4)

Animation depicting an event of CH_4 dissociation around a Ni and a Bi atom (MP4)

Animation depicting an event of CH_4 dissociation around a Ni and a Cu atom (MP4)

Animation depicting an event of CH_4 dissociation with the contribution of several atoms (MP4)

■ AUTHOR INFORMATION

Corresponding Author

Hande Ustunel − *Department of Physics, Middle East Technical University, 06800 Ankara, Turkey;* orcid.org/0000-0003-0307-9036; Email: ustunel@metu.edu.tr

Authors

Arda Erbasan − *Department of Physics, Middle East Technical University, 06800 Ankara, Turkey*

Daniele Toffoli − *Dipartimento di Scienze Chimiche e Farmaceutiche, Università degli Studi di Trieste, I-34127 Trieste, Italy; IOM-CNR, Istituto Officina dei Materiali-CNR, 34149 Trieste, Italy;* orcid.org/0000-0002-8225-6119

Iskender Gokalp − *Tübitak Marmara Research Center, 41470 Gebze, Kocaeli, Turkey*

Gulfeza Kardas − *Chemistry Department Arts and Sciences Faculty, Cukurova University, 01250 Saricam, Adana, Turkey*

Gokhan Celik − *Department of Chemical Engineering, Middle East Technical University, 06800 Ankara, Turkey;* orcid.org/0000-0001-8070-5219

Complete contact information is available at: https://pubs.acs.org/10.1021/acsaem.3c03235

Notes

The authors declare no competing financial interest.

■ ACKNOWLEDGMENTS

This work was financially supported by the Scientific and Technological Research Council of Türkiye (TÜBİTAK), Grant no: 121M443. A.E. and H.U. acknowledge the computational resources provided by the National High-Performance Center TÜBİTAK-TRUBA.

■ REFERENCES

(1) Dincer, I.; Acar, C. Review and evaluation of hydrogen production methods for better sustainability. *Int. J. Hydrogen Energy* **2015**, *40*, 11094−11111.

(2) Serra, J. M.; Borrás-Morell, J. F.; García-Baños, B.; Balaguer, M.; Plaza-González, P.; Santos-Blasco, J.; Catalán-Martínez, D.; Navarrete, L.; Catalá-Civera, J. M. Hydrogen production via microwave-induced water splitting at low temperature. *Nat. Energy* **2020**, *5*, 910−919.

(3) Meramo-Hurtado, S. I.; Puello, P.; Cabarcas, A. Process Analysis of Hydrogen Production via Biomass Gasification under Computer-Aided Safety and Environmental Assessments. *ACS Omega* **2020**, *5*, 19667−19681.

(4) Boretti, A.; Banik, B. K. Advances in Hydrogen Production from Natural Gas Reforming. *Adv. Energy Sustainability Res.* **2021**, *2*, 2100097.

(5) Abdin, Z.; Zafaranloo, A.; Rafiee, A.; Mérida, W.; Lipiński, W.; Khalilpour, K. R. Hydrogen as an energy vector. *Renewable Sustainable Energy Rev.* **2020**, *120*, 109620.
(6) *Global Hydrogen Review*, 2023. https://www.iea.org/reports/global-hydrogen-review-2023.
(7) Nikolaidis, P.; Poullikkas, A. A comparative overview of hydrogen production processes. *Renewable Sustainable Energy Rev.* **2017**, *67*, 597−611.
(8) Baykara, S. Z. Hydrogen: A brief overview on its sources, production and environmental impact. *Int. J. Hydrogen Energy* **2018**, *43*, 10605−10614.
(9) Sánchez-Bastardo, N.; Schlögl, R.; Ruland, H. Methane Pyrolysis for CO2-Free H2 Production: A Green Process to Overcome Renewable Energies Unsteadiness. *Chem. Ing. Tech.* **2020**, *92*, 1596−1609.
(10) Sánchez-Bastardo, N.; Schlögl, R.; Ruland, H. Methane Pyrolysis for Zero-Emission Hydrogen Production: A Potential Bridge Technology from Fossil Fuels to a Renewable and Sustainable Hydrogen Economy. *Ind. Eng. Chem. Res.* **2021**, *60*, 11855−11881.
(11) Chen, C.-J.; Back, M. H.; Back, R. A. The thermal decomposition of methane. II. Secondary reactions, autocatalysis and carbon formation; non-Arrhenius behaviour in the reaction of CH3 with ethane. *Can. J. Chem.* **1976**, *54*, 3175−3184.
(12) Roscoe, J. M.; Thompson, M. J. Thermal decomposition of methane: Autocatalysis. *Int. J. Chem. Kinet.* **1985**, *17*, 967−990.
(13) Alstrup, I.; Tavares, M. T. The kinetics of carbon formation from CH4 + H2 on a silica-supported nickel catalyst. *J. Catal.* **1992**, *135*, 147−155.
(14) Wang, I. W.; Kutteri, D. A.; Gao, B.; Tian, H.; Hu, J. Methane Pyrolysis for Carbon Nanotubes and CO_x-Free H_2 over Transition-Metal Catalysts. *Energy Fuels* **2019**, *33*, 197−205.
(15) Jana, P.; O'Shea, V. A. D. L. P.; Coronado, J. M.; Serrano, D. P. Mild temperature hydrogen production by methane decomposition over cobalt catalysts prepared with different precipitating agents. **2012**, 7034−7041.
(16) Amin, A.; Epling, W.; Croiset, E. Reaction and Deactivation Rates of Methane Catalytic Cracking over Nickel. *Ind. Eng. Chem. Res.* **2011**, *50*, 12460−12470.
(17) Vlaskin, M.; Grigorenko, A.; Gromov, A.; Kumar, V.; Dudoladov, A.; Slavkina, O.; Darishchev, V. Methane pyrolysis on sponge iron powder for sustainable hydrogen production. *Results Eng.* **2022**, *15*, 100598.
(18) Liu, B.; Lyu, S.; Lee, T.; Choi, S.; Eum, S.; Yang, C.; Park, C.; Lee, C. Synthesis of single- and double-walled carbon nanotubes by catalytic decomposition of methane. *Chem. Phys. Lett.* **2003**, *373*, 475−479.
(19) Syed Muhammad, A. F.; Awad, A.; Saidur, R.; Masiran, N.; Salam, A.; Abdullah, B. Recent advances in cleaner hydrogen productions via thermo-catalytic decomposition of methane: Admixture with hydrocarbon. *Int. J. Hydrogen Energy* **2018**, *43*, 18713−18734.
(20) Chen, L.; Qi, Z.; Zhang, S.; Su, J.; Somorjai, G. A. Catalytic Hydrogen Production from Methane: A Review on Recent Progress and Prospect. *Catalysts* **2020**, *10*, 858.
(21) Wang, H. Y.; Lua, A. C. Development of metallic nickel nanoparticle catalyst for the decomposition of methane into hydrogen and carbon nanofibers. *J. Phys. Chem. C* **2012**, *116*, 26765−26775.
(22) Hasnan, N. S. N.; Timmiati, S. N.; Pudukudy, M.; Yaakob, Z.; Lim, K. L.; Taufiq-Yap, Y. H. Catalytic decomposition of methane into hydrogen and carbon nanotubes over mesostructured silica nanoparticle-supported nickel catalysts. *J. Porous Mater.* **2020**, *27*, 369−382.
(23) Pudukudy, M.; Yaakob, Z.; Jia, Q.; Takriff, M. S. Catalytic decomposition of methane over rare earth metal (Ce and La) oxides supported iron catalysts. *Appl. Surf. Sci.* **2019**, *467−468*, 236−248.
(24) Hasnan, N. S. N.; Pudukudy, M.; Yaakob, Z.; Kamarudin, N. H. N.; Lim, K. L.; Timmiati, S. N. Promoting Effects of Copper and Iron on Ni/MSN Catalysts for Methane Decomposition. *Catalysts* **2023**, *13*, 1067.
(25) Steinberg, M. Fossil fuel decarbonization technology for mitigating global warming. *Int. J. Hydrogen Energy* **1999**, *24*, 771−777.
(26) Serban, M.; Lewis, M. A.; Marshall, C. L.; Doctor, R. D. Hydrogen Production by Direct Contact Pyrolysis of Natural Gas. *Energy Fuels* **2003**, *17*, 705−713.
(27) Wang, K.; Li, W.; Zhou, X. Hydrogen generation by direct decomposition of hydrocarbons over molten magnesium. *J. Mol. Catal. A: Chem.* **2008**, *283*, 153−157.
(28) Plevan, M.; Geißler, T.; Abánades, A.; Mehravaran, K.; Rathnam, R.; Rubbia, C.; Salmieri, D.; Stoppel, L.; Stückrad, S.; Wetzel, T. Thermal cracking of methane in a liquid metal bubble column reactor: Experiments and kinetic analysis. *Int. J. Hydrogen Energy* **2015**, *40*, 8020−8033.
(29) Schultz, I.; Agar, D. W. Decarbonisation of fossil energy via methane pyrolysis using two reactor concepts: Fluid wall flow reactor and molten metal capillary reactor. *Int. J. Hydrogen Energy* **2015**, *40*, 11422−11427.
(30) Geißler, T.; Plevan, M.; Abánades, A.; Heinzel, A.; Mehravaran, K.; Rathnam, R.; Rubbia, C.; Salmieri, D.; Stoppel, L.; Stückrad, S.; Weisenburger, A.; Wenninger, H.; Wetzel, T. Experimental investigation and thermo-chemical modeling of methane pyrolysis in a liquid metal bubble column reactor with a packed bed. *Int. J. Hydrogen Energy* **2015**, *40*, 14134−14146.
(31) Geißler, T.; Abánades, A.; Heinzel, A.; Mehravaran, K.; Müller, G.; Rathnam, R.; Rubbia, C.; Salmieri, D.; Stoppel, L.; Stückrad, S.; Weisenburger, A.; Wenninger, H.; Wetzel, T. Hydrogen production via methane pyrolysis in a liquid metal bubble column reactor with a packed bed. *Chem. Eng. J.* **2016**, *299*, 192−200.
(32) Korányi, T. I.; Németh, M.; Beck, A.; Horváth, A. Recent Advances in Methane Pyrolysis: Turquoise Hydrogen with Solid Carbon Production. *Energies* **2022**, *15*, 6342.
(33) Leal Pérez, B. J.; Medrano Jiménez, J. A.; Bhardwaj, R.; Goetheer, E.; van Sint Annaland, M.; Gallucci, F. Methane pyrolysis in a molten gallium bubble column reactor for sustainable hydrogen production: Proof of concept & techno-economic assessment. *Int. J. Hydrogen Energy* **2021**, *46*, 4917−4935.
(34) Parkinson, B.; Matthews, J. W.; McConnaughy, T. B.; Upham, D. C.; McFarland, E. W. Techno-Economic Analysis of Methane Pyrolysis in Molten Metals: Decarbonizing Natural Gas. *Chem. Eng. Technol.* **2017**, *40*, 1022−1030.
(35) Upham, D. C.; Agarwal, V.; Khechfe, A.; Snodgrass, Z. R.; Gordon, M. J.; Metiu, H.; McFarland, E. W. Catalytic molten metals for the direct conversion of methane to hydrogen and separable carbon. *Science* **2017**, *358*, 917−921.
(36) Palmer, C.; Tarazkar, M.; Kristoffersen, H. H.; Gelinas, J.; Gordon, M. J.; McFarland, E. W.; Metiu, H. Methane Pyrolysis with a Molten Cu−Bi Alloy Catalyst. *ACS Catal.* **2019**, *9*, 8337−8345.
(37) Zeng, J.; Tarazkar, M.; Pennebaker, T.; Gordon, M. J.; Metiu, H.; McFarland, E. W. Catalytic Methane Pyrolysis with Liquid and Vapor Phase Tellurium. *ACS Catal.* **2020**, *10*, 8223−8230.
(38) Zaghloul, N.; Kodama, S.; Sekiguchi, H. Hydrogen Production by Methane Pyrolysis in a Molten-Metal Bubble Column. *Chem. Eng. Technol.* **2021**, *44*, 1986−1993.
(39) Scheiblehner, D.; Neuschitzer, D.; Wibner, S.; Sprung, A.; Antrekowitsch, H. Hydrogen production by methane pyrolysis in molten binary copper alloys. *Int. J. Hydrogen Energy* **2023**, *48*, 6233−6243.
(40) Kim, J.; Oh, C.; Oh, H.; Lee, Y.; Seo, H.; Kim, Y. K. Catalytic methane pyrolysis for simultaneous production of hydrogen and graphitic carbon using a ceramic sparger in a molten NiSn alloy. *Carbon* **2023**, *207*, 1−12.
(41) Joo, S.; Kim, K.; Kwon, O.; Oh, J.; Kim, H. J.; Zhang, L.; Zhou, J.; Wang, J.-Q.; Jeong, H. Y.; Han, J. W.; Kim, G. Enhancing Thermocatalytic Activities by Upshifting the d-Band Center of Exsolved Co-Ni-Fe Ternary Alloy Nanoparticles for the Dry Reforming of Methane. *Angew. Chem., Int. Ed.* **2021**, *60*, 15912−15919.
(42) Kareem, H.; Maswadeh, Y.; Wu, Z.-P.; Leff, A. C.; Cheng, H.-W.; Shan, S.; Wang, S.; Robinson, R.; Caracciolo, D.; Langrock, A.;

Mackie, D. M.; Tran, D. T.; Petkov, V.; Zhong, C.-J. Lattice Strain and Surface Activity of Ternary Nanoalloys under the Propane Oxidation Condition. *ACS Appl. Mater. Interfaces* **2022**, *14*, 11435−11447.
(43) Zhang, L.; Meng, Y.; Xie, B.; Xia, S. Theoretical investigation onto the reaction mechanism of dry reforming of methane on core−shell Cu-Ni-Pt ternary alloy clusters. *Chem. Phys. Lett.* **2021**, *781*, 138975.
(44) Maluf, S.; Assaf, E. Ni catalysts with Mo promoter for methane steam reforming. *Fuel* **2009**, *88*, 1547−1553.
(45) Saraswat, S.; Pant, K. Ni−Cu−Zn/MCM-22 catalysts for simultaneous production of hydrogen and multiwall carbon nanotubes via thermo-catalytic decomposition of methane. *Fuel Energy Abstr.* **2011**, *36*, 13352−13360.
(46) Bhattacharjee, S.; Waghmare, U. V.; Lee, S. C. An improved d-band model of the catalytic activity of magnetic transition metal surfaces. *Sci. Rep.* **2016**, *6*, 35916.
(47) Li, Z.; Xu, J.; Gu, X.; Wang, K.; Wang, W.; Zhang, X.; Zhang, Z.; Ding, Y. Selective Gas-Phase Oxidation of Alcohols over Nanoporous Silver. *ChemCatChem* **2013**, *5*, 1705−1708.
(48) Cheng, Z.; Fine, N. a.; Lo, C. S. Platinum Nanoclusters Exhibit Enhanced Catalytic Activity for Methane Dehydrogenation. *Top. Catal.* **2012**, *55*, 345−352.
(49) Wang, B.; Tao, L.; Cheng, Y.; Yang, F.; Jin, Y.; Zhou, C.; Yu, H.; Yang, Y. Electrocatalytic Oxidation of Small Molecule Alcohols over Pt, Pd, and Au Catalysts: The Effect of Alcohol's Hydrogen Bond Donation Ability and Molecular Structure Properties. *Catalysts* **2019**, *9*, 387.
(50) Zhu, X.; Guo, Q.; Sun, Y.; Chen, S.; Wang, J. Q.; Wu, M.; Fu, W.; Tang, Y.; Duan, X.; Chen, D.; Wan, Y. Optimising surface d charge of AuPd nanoalloy catalysts for enhanced catalytic activity. *Nat. Commun.* **2019**, *10*, 1428.
(51) Zhang, J.; She, Y. Mechanism of methanol decomposition on the Pd/WC(0001) surface unveiled by first-principles calculations. *Front. Chem. Sci. Eng.* **2020**, *14*, 1052−1064.
(52) Henkelman, G.; Uberuaga, B. P.; Jónsson, H. A climbing image nudged elastic band method for finding saddle points and minimum energy paths. *J. Chem. Phys.* **2000**, *113*, 9901−9904.
(53) Palmer, C.; Tarazkar, M.; Gordon, M. J.; Metiu, H.; McFarland, E. W. Methane pyrolysis in low-cost, alkali-halide molten salts at high temperatures. *Sustainable Energy Fuels* **2021**, *5*, 6107−6123.
(54) Zeng, J.; Tarazkar, M.; Palmer, C.; Gordon, M. J.; Metiu, H.; McFarland, E. W. Initial Steps in CH4 Pyrolysis on Cu and Ni. *J. Phys. Chem. C* **2021**, *125*, 18665−18672.
(55) Bae, D.; Kim, Y.; Ko, E. H.; Ju Han, S.; Lee, J. W.; Kim, M.; Kang, D. Methane pyrolysis and carbon formation mechanisms in molten manganese chloride mixtures. *Appl. Energy* **2023**, *336*, 120810.
(56) Chen, L.; Song, Z.; Zhang, S.; Chang, C.-K.; Chuang, Y.-C.; Peng, X.; Dun, C.; Urban, J. J.; Guo, J.; Chen, J.-L.; Prendergast, D.; Salmeron, M.; Somorjai, G. A.; Su, J. Ternary NiMo-Bi liquid alloy catalyst for efficient hydrogen production from methane pyrolysis. *Science* **2023**, *381*, 857−861.
(57) Miyazawa, K.; Tanaka, Y. LAMMPS molecular dynamics simulation of methane decomposition on nickel thin films at high temperatures. *Surf. Sci.* **2021**, *713*, 121904.
(58) Kresse, G.; Hafner, J. Ab initio molecular dynamics for liquid metals. *Phys. Rev. B* **1993**, *47*, 558−561.
(59) Kresse, G.; Furthmüller, J. Efficiency of ab-initio total energy calculations for metals and semiconductors using a plane-wave basis set. *Comput. Mater. Sci.* **1996**, *6*, 15−50.
(60) Kresse, G.; Furthmüller, J. Efficient iterative schemes for ab initio total-energy calculations using a plane-wave basis set. *Phys. Rev. B: Condens. Matter Mater. Phys.* **1996**, *54*, 11169−11186.
(61) Perdew, J. P.; Burke, K.; Ernzerhof, M. Generalized Gradient Approximation Made Simple. *Phys. Rev. Lett.* **1996**, *77*, 3865−3868.
(62) Blöchl, P. E. Projector augmented-wave method. *Phys. Rev. B: Condens. Matter Mater. Phys.* **1994**, *50*, 17953−17979.
(63) Kresse, G.; Joubert, D. From ultrasoft pseudopotentials to the projector augmented-wave method. *Phys. Rev. B: Condens. Matter Mater. Phys.* **1999**, *59*, 1758−1775.
(64) Grimme, S.; Antony, J.; Ehrlich, S.; Krieg, H. A consistent and accurate ab initio parametrization of density functional dispersion correction (DFT-D) for the 94 elements H-Pu. *J. Chem. Phys.* **2010**, *132*, 154104.
(65) Martinez, L.; Andrade, R.; Birgin, E. G.; Martínez, J. M. PACKMOL: A package for building initial configurations for molecular dynamics simulations. *J. Comput. Chem.* **2009**, *30*, 2157−2164.
(66) Truhlar, D. G.; Garrett, B. C.; Klippenstein, S. J. Current Status of Transition-State Theory. *J. Phys. Chem.* **1996**, *100*, 12771−12800.
(67) Han, Y.; Hobbie, E. K.; Kilin, D. S. First-Principles Molecular Dynamics of Monomethylhydrazine and Nitrogen Dioxide. *J. Phys. Chem. Lett.* **2019**, *10*, 2394−2399.
(68) Tang, W.; Sanville, E.; Henkelman, G. A grid-based Bader analysis algorithm without lattice bias. *J. Phys.: Condens. Matter* **2009**, *21*, 084204.
(69) Tiwari, M.; Mandal, S. C.; Das, A.; Pathak, B. Subsurface Li Monolayer on Cu(111) Surfaces for Upgrading Ethanol to n-Butanol: A Computational Study. *ACS Appl. Nano Mater.* **2023**, *6*, 7156−7165.
(70) Parnis, J. M.; Ozin, G. A. Photochemical activation of methane by aluminum atoms: Al + CH4.dblarw. CH3AlH, a photoreversible reaction. *J. Am. Chem. Soc.* **1986**, *108*, 1699−1700.
(71) Varghese, J. J.; Mushrif, S. H. First-principles investigation of the dissociation and coupling of methane on small copper clusters: Interplay of collision dynamics and geometric and electronic effects. *J. Chem. Phys.* **2015**, *142*, 184308.
(72) Roy, S.; Hariharan, S.; Tiwari, A. K. Pt−Ni Subsurface Alloy Catalysts: An Improved Performance toward CH4 Dissociation. *J. Phys. Chem. C* **2018**, *122*, 10857−10870.
(73) Niu, J.; Zhang, C.; Liu, H.; Jin, Y.; Zhang, R.; Ran, J. Unraveling the effects of Ni particle size and facet on CH4 activation: From cluster to nanoparticle. *Int. J. Hydrogen Energy* **2023**, *48*, 19486−19493.
(74) Boo, J.; Lee, S. J.; Park, N.-K.; Kim, M.; Kang, D. Catalytic decomposition of NO using molten gallium: an experimental and computational study. *Mol. Catal.* **2023**, *543*, 113144.
(75) Lefort, P.; Tetard, D.; Tristant, P. Formation of aluminium carbide by carbothermal reduction of alumina: Role of the gaseous aluminium phase. *J. Eur. Ceram. Soc.* **1993**, *12*, 123−129.
(76) Niu, J.; Liu, H.; Jin, Y.; Fan, B.; Qi, W.; Ran, J. A density functional theory study of methane activation on MgO supported Ni9M1 cluster: role of M on C-H activation. *Front. Chem. Sci. Eng.* **2022**, *16*, 1485−1492.

https://doi.org/10.1021/acsaem.3c03235
ACS Appl. Energy Mater. 2024, 7, 3220−3233